Soft Matter

PAPER

View Article Online
View Journal | View Issue

Cite this: *Soft Matter*, 2021, **17**, 1963

Penetration and preferential binding of charged nanoparticles to mixed lipid monolayers: interplay of lipid packing and charge density†

Anurag Chaudhury, [a] Koushik Debnath, [b] Wei Bu,[c] Nikhil R. Jana [b] and Jaydeep Kumar Basu *[a]

Received 31st October 2020,
Accepted 14th December 2020

DOI: 10.1039/d0sm01945c

rsc.li/soft-matter-journal

Designing of nanoparticles (NPs) for biomedical applications or mitigating their cytotoxic effects requires microscopic understanding of their interactions with cell membranes. Such insight is best obtained by studying model biomembranes which, however, need to replicate actual cell membranes, especially their compositional heterogeneity and charge. In this work we have investigated the role of lipid charge density and packing of phase separated Langmuir monolayers in the penetration and phase specificity of charged quantum dot (QD) binding. Using an ordered and anionic charged lipid in combination with uncharged but variable stiffness lipids we demonstrate how the subtle interplay of zwitterionic lipid packing and anionic lipid charge density can affect cationic nanoparticle penetration and phase specific binding. Under identical subphase pH, the membrane with higher anionic charge density displays higher NP penetration. We also observe coalescence of charged lipid rafts floating amidst a more fluidic zwitterionic lipid matrix due to the phase specificity of QD binding. Our results suggest effective strategies which can be used to design NPs for diverse biomedical applications as well as to devise remedial actions against their harmful cytotoxic effects especially against respiratory diseases.

1 Introduction

Various forms of designer and functional nanoparticles (NPs) have been developed as nanoprobes for various biomedical applications including bioimaging probes, drug delivery carriers and theranostics among others.[1–10] In particular, fluorescent NPs like quantum dots (QDs) having high quantum efficiency are very suitable for *in vitro* and small animal imaging in general and single molecule imaging applications in complex bioenvironments in particular. It is also well known that the cell–nanoparticle interaction is highly sensitive to the NP surface chemistry and surface charge[11–17] and hence the nanoprobe surface must be appropriately designed for the purpose for which it is meant to be used. For example NPs designed for binding to specific receptors on the cell surface or on the cell membrane in general will not be suitable for sub-cellular targeting. In this regard it has been further revealed by us earlier[2,18] that NP uptake by cells can follow the membrane raft-mediated pathway or the receptor mediated pathway by subtle tuning of surface properties of NPs. Similarly, NPs can have pH dependent functionality which can alter their effectiveness in interactions with cells or intracellular organelles.[10,19–22] Cancerous cells, in particular, are known to have a dysregulated pH gradient with a lower extracellular pH.[23,24] So it is important to understand the role of the electrolytic environment in affecting the NP–membrane interaction. To target healthy cells or for bio-imaging purpose, the penetration of these NPs inside the membranes is undesirable whereas for cancerous cells, endocytosis of these NPs may be required for hyperthermia treatment or chemical pyrolysis inside cancer cells.[25–30] The second aspect of NP-cell interactions, pertaining to NP endocytosis is especially significant in the context of interaction of NPs with lung surfactant monolayer due to inhalation of such particles and their deposition in the alveolar region of the lung leading to severe respiratory diseases.[31–36] *In vitro* studies, which seek to explore the efficiency of nanoparticles for various targeted nano–biotechnological applications or their possible adverse effects on different cells, are necessary in developing improved nanoparticle designs or in remedial actions against their bio-hazardous properties.[11,37] However, due to the inherent complexity of various cell membranes, a large variability in toxicity and permeation efficiency is often observed for NPs in different cell lines.[37–39] Therefore, the

[a] *Department of Physics, Indian Institute of Science, Bangalore 560012, India. E-mail: basu@iisc.ac.in; Tel: +91 080 2293 3281*
[b] *School of Materials Science, Indian Association for the Cultivation of Science, Kolkata-700032, India*
[c] *NSF's ChemMatCARS, University of Chicago, Chicago, IL 60637, USA*

† Electronic supplementary information (ESI) available. See DOI: 10.1039/d0sm01945c

derivation of general principles and factors determining NP interactions and permeability of cellular membranes from *in vitro* studies is non-trivial. In this regard, fundamental studies that could mimic the interaction of NPs with biomembranes in a simplified and highly controlled environment are very important in obtaining microscopic insight.

While hydrophobic, hydrophilic as well as charged (both cationic and anionic) NPs have been designed with the goal of enabling specific applications, charged NPs have been generally found to be more effective in cell membrane penetration due to the predominantly anionic charge of most cell membranes. In the context of charged NPs interacting with model biomembranes, supported lipid bilayers (SLBs)[40–47] and monolayer membranes at the air–water interface[41,48–52] have been extensively used to explore the nature of interactions. Several studies have focused on the effects of NPs on the fluidity of SLBs reporting either their softening or stiffening depending on the various parameters of the NPs such as size and shape or charge.[12,13,45,53–55] Most studies have focused on single component[9,12,15,50,51,56–58] lipid membranes of various degrees of stiffness. However, recent studies including experiments[18,43,59,60] and molecular dynamics (MD) simulations[61] have suggested enhanced and/or phase-specific binding of charged NPs in multicomponent zwitterionic lipid membranes having coexisting liquid ordered (L_o) and disordered (L_d) phases. Experiments[18,44,59] and MD simulations[61] suggest preferential binding to the L_d phase and also enhanced binding at the phase boundary. In fact our recent studies, using super-resolution stimulated emission depletion (STED) microscopy, depicted the key role played by dynamical membrane nanodomains in determining NP interaction and binding.[18,62] As mentioned earlier, most cellular membranes including the lung surfactant on lung alveolar cells not only contain lipid compositional heterogeneity but also necessarily contain charged (mostly anionic) lipids. Hence, a more realistic understanding of NP–cell interactions in *in vitro* studies can be provided with the use of both phase separated and mixed charged–uncharged lipid based biomimetic membranes. However, very little work has been reported[31,63] on charged NP interactions with mixed charged–uncharged lipid membranes.

In this work, we report on *in situ* grazing incidence X-ray scattering (GIXS) studies on the nature of cationic NP binding and permeability in two-component, nanoscale phase separated, Langmuir monolayers consisting of mixtures of anionic and zwitterionic lipids of different stiffness, at the air–water interface. The charged NPs used in this study consist of cadmium selenide (CdSe)/zinc sulphide (ZnS) core–shell quantum dots (QDs). We studied two different lipid monolayer compositions in which the anionic lipid component, (1,2-dipalmitoyl-*sn-glycero*-3-phospho-(1-*rac*-glycerol) (sodium salt) (DPPG), which exists in a highly ordered state, was fixed, while the stiffness of the zwitterionic lipid as well as the lipid charge density was systematically varied. Detailed analysis of X-ray reflectivity (XR) data from the lipid monolayers suggests that cationic Quantum Dot (CQD) penetration is maximum for monolayers with fluidic zwitterionic (DOPC – 1,2-dioleyl-*sn-glycero*-3-phosphocholine, denoted O1G1) lipids on water (pH = 6) although the NP coverage is lower compared to an identical monolayer on a PBS (phosphate-buffered-saline) subphase (pH = 7). Despite the higher CQD surface coverage underneath the O1G1 monolayer on the PBS subphase compared to that on water, we did not observe higher penetration of identical CQDs due to their reduced surface charge at higher pH. However, interestingly, we observed clear evidence of preferential binding of CQDs to the ordered and charged phase of the monolayer (consisting mostly of DPPG) as evidenced from the increased headgroup thickness of the DPPG lipids. Completely opposite behaviour was observed for the monolayer with a stiffer zwitterionic lipid (DPPC – 1,2-dipalmitoyl-*sn-glycero*-3-phosphocholine), denoted P2G1, on PBS. There seems to be partial penetration of CQDs into the monolayer and the preferential phase selectivity is weaker with the lipid headgroup sizes reducing instead of increasing as in O1G1. Grazing incidence X-ray diffraction (GID) studies revealed subtle effects in terms of how the CQDs interact with the monolayers as evidenced from the changes in the ordered nanodomain sizes. For O1G1 on water the raft-like L_o nanodomains, consisting predominantly DPPG lipids, considerably shrink in size due to CQD binding and strong penetration while for O1G1 on PBS we observe nanodomain coarsening which is consistent with increased headgroup size and out-of-plane coherence length. Our results provide microscopic insight into the subtle interplay of packing and charge density of lipids along with nanoparticle charge which determine the penetration, phase selective binding and interaction of NPs with cell membranes which can help in several aspects in designing NPs for their nano-biotechnological applications in drug delivery, bioimaging as well as in mitigating their cytotoxic effects.

2 Experimental details

2.1 Materials

1,2-Dipalmitoyl-*sn-glycero*-3-phosphocholine (DPPC), 1,2-dioleyl-*sn-glycero*-3-phosphocholine (DOPC) and 1,2-dipalmitoyl-*sn-glycero*-3-phospho-(1-*rac*-glycerol) (sodium salt) (DPPG) phospholipids were purchased from Avanti polar lipids. HPLC grade chloroform was purchased from Sigma-Aldrich and used to prepare the stock solution of the phospholipids. Sodium dihydrogen phosphate (NaH_2PO4), disodium hydrogen phosphate (Na_2HPO_4), potassium chloride (KCl) and sodium chloride (NaCl) were purchased from Sigma-Aldrich and used to prepare phosphate buffer solution. The buffer was maintained at a pH of 7. Ultrapure deionized water with a resistivity of 18.2 MΩ cm was used to prepare the buffer solution as well as the subphase for the monolayer studies. Red emissive cationic core/shell quantum dots (QDs) of average hydrodynamic diameter 22 nm with cadmium selenide core and zinc sulphide shell were prepared according to our previously reported method.[64] The QDs were made hydrophilic *via* polyacrylate coating by using acrylate monomeric ligands. The synthesis protocol along with their characterization is available in the ESI.†

2.2 Methods

Lipid solutions were prepared for DOPC, DPPC and DPPG in spectrograde chloroform. The lipids stocks were mixed to prepare DOPC : DPPG = 1 : 1 or DPPC : DPPG = 2 : 1 solutions. DOPC : DPPG (1 : 1) or DPPC : DPPG (2 : 1) were spread onto the aqueous subphase (volume of 320 mL) of an 8.9 cm × 42 cm Langmuir trough (Nima Technology Ltd, Coventry, England) maintained at 20.0 ± 0.5 °C. The subphase was either deionized (DI) water having pH 6 or a freshly prepared and filtered Phosphate Buffered Saline (PBS) maintained at pH 7. The surface pressure was measured with a precision of 0.1 mN m^{-1} using a Wilhelmy balance and a Whatman filter paper Wilhemy plate. After solvent evaporation (15 min), the monolayer was compressed and expanded once with a barrier speed of 7.5 cm^2 min^{-1} in order to create a homogeneous floating Langmuir film. Between measurements with NPs, the Langmuir–Blodgett (LB) trough was cleaned thrice with ethanol (95%), twice with DI water and once with chloroform. Addition of 10 nM CQDs was carried out using a micro-pipette to inject the CQD aliquot from outside the barriers into the subphase with the mixed monolayer in a compressed state having a surface pressure of 26 mN m^{-1} and maintained at a subphase temperature of 20 °C. The subphase was then gently stirred for 10–15 minutes using an L-shaped stirrer, without disturbing the compressed monolayer, to properly mix the CQDs in the subphase. X-ray measurements were carried out after stabilized dissolution of the CQDs.

2.3 Grazing incidence X-ray scattering (GIXS)

The GIXS experiments were performed at beamline 15-ID-C ChemMatCARS at the Advanced Photon Source (APS) at Argonne National Laboratory with the following parameters: X-ray beam wavelength, λ, of 1.239 Å, and horizontal and vertical beam size of 2 mm and 20 μm, respectively, leading to a beam footprint of 2 mm × 1.26 cm. The detector used was PILATUS 100 K (Dectris) set to single-photon counting mode. Two sets of slits, one placed in front of the detector and the other placed 280 mm from the sample, were used to minimize intense low-angle scattering. For GIXS experiments, the sample was enclosed within a box and purged with helium to avoid water vapour accumulation which will attenuate the scattered signal from the sample, and the oxygen level was kept below 2% to avoid radiation damage of the lipids. During the measurements, the sample was horizontally translated by 2 mm to a fresh location at regular intervals to avoid prolonged beam exposure.

2.3.1 X-ray reflectivity (XR). The XR experiments on the pristine monolayers were performed at a lateral surface pressure of 32 mN m^{-1} and 26 mN m^{-1} at a temperature of 20.0 ± 0.5 °C and after adding the CQDs while maintaining a constant surface pressure of 26 mN m^{-1}. XR was measured as a function of the vertical scattering vector component ($\mathbf{q}_z$). XR probes the electron density variation $\rho(z)$ of the vertical structure of the layers normal to the air/water interface. The coherent scattering length density (SLD), $\rho_s(z)$, distribution, normal to a sample's surface and averaged over the footprint of the beam on the sample, was obtained through the analysis of specular reflectometry data. $\rho_s(z)$ is a value unique to a particular chemical composition and is proportional to the mass density and thereby the electron density. A slab model was used to represent the monolayer as a stack of slabs, with each slab having a constant thickness and electron density or SLD. The $\rho_s(z)$ profile was laterally averaged over both the ordered and disordered parts of the monolayer under the footprint of the X-ray beam and was calculated by a sum of error functions as

$$\rho_s(z) = \frac{1}{2}\sum_{n=0}^{N-1} \mathrm{erf}\left(\frac{z - z_i}{\sqrt{2}\sigma}\right)\left(\rho_{s_{i+1}} - \rho_{s_i}\right) + \frac{\rho_{s_0} + \rho_{s_N}}{2}, \qquad (1)$$

where $\mathrm{erf}(z) = 2/\sqrt{\pi}\int_0^z e^{-t^2} dt$, σ is the surface roughness from capillary wave theory, N is the number of internal interfaces, z_i is the position of the ith interface, ρ_{s_i} is the SLD of the ith interface, and ρ_{s_0} is the SLD of the aqueous subphase. Modeling of $\rho_s(z)$ was performed using an open-source reflectivity package, MOTOFIT, which runs in the IGOR Pro environment.[65] Using the recursive Parratt formalism,[66] a theoretical reflectometry curve can be calculated and compared to the measured data. Both genetic optimization and Levenberg–Marquardt nonlinear least-squares methods were employed to obtain the best fits with the lowest χ^2 values and structurally meaningful model parameters.

2.3.2 Grazing incidence diffraction (GID). For GID experiments the incidence angle was kept fixed at 0.0906° while all other parameters were the same as for XR measurements. The measured GID data are plotted as contour plots of the intensity as a function of both the horizontal ($\mathbf{q}_{xy}$) and the vertical ($\mathbf{q}_z$) scattering vector components. The lattice spacing d_{hk} was obtained from the in-plane diffraction data as $d_{hk} = 2\pi/\mathbf{q}_{xy}^{hk}$, where the Miller indices h, k were used to index the Bragg peaks needed to calculate the unit cell parameters for the in-plane lattice. The full width at half maximum (fwhm) of the Bragg peaks after correction for the instrumental resolution (0.012 $Å^{-1}$) was used to calculate the in-plane correlation length using the Scherrer formula[67] as follows:

$$L_{xy} \approx 0.9 \times 2\pi/\mathrm{fwhm}_{\mathrm{intrinsic}}(\mathbf{q}_{xy}) \qquad (2)$$

where

$$\mathrm{fwhm}_{\mathrm{intrinsic}}(\mathbf{q}_{xy}) = [\mathrm{fwhm}_{\mathrm{measured}}(\mathbf{q}_{xy})^2 - \mathrm{fwhm}_{\mathrm{resolution}}(\mathbf{q}_{xy})^2]^{1/2}. \qquad (3)$$

The fwhm of the Bragg rods was used to estimate the vertical correlation length as $L \approx 0.9 \times 2\pi/\mathrm{fwhm}(\mathbf{q}_z)$.[68] The GID experiments on the pristine monolayers were performed at two lateral surface pressures of 32 mN m^{-1} and 26 mN m^{-1} and at a temperature of 20.0 ± 0.5 °C. After adding CQDs, GID data were collected while maintaining a constant surface pressure of 26 mN m^{-1}.

2.3.3 X-ray fluorescence (XRF). X-ray fluorescence (XRF) measurements were carried out in GID geometry at incident angles $\mathbf{q}_z < \mathbf{q}_c$ (critical angle of X-rays for the air–water interface). A Vortex-60EX multi-cathode energy dispersive X-ray detector (SII Nano Technology USA, Inc.) was placed in a

cylindrical well above the interface. It collects fluorescent X-rays from the sample through a Kapton window that caps the bottom of the cylindrical well. The details about the technique can be found in an earlier report.[69]

3 Results and discussion

3.1 X-ray reflectivity measurements

Fig. 1(a) shows normalized XR data and the corresponding fitted profiles for O1G1 FLMs on water before and after incubation with CQDs in the subphase. The extracted $\rho_s(z)$ profiles of the monolayers corresponding to the best fit in Fig. 1a are presented in Fig. 1b. The main observations that can be gleaned from $\rho_s(z)$ for the pristine O1G1 monolayer are that merely one head and tail layer does not fit the data well (Fig. 1a, pink solid line), and it is necessary to include two tail and head layers each, which is typical for raft-like lipid monolayers consisting of L_o–L_d phases as observed earlier.[70,71] The DOPC lipid forms the L_d phase and has lower thickness compared to the DPPG lipids which constitute the L_o phase as reported earlier,[72,73] leading to a height difference, ΔH, of 3.67 Å. On addition of CQDs, the calculated XR profiles in Fig. 1(a) clearly show the need for an additional layer below (in the subphase) and a low density layer above the monolayer (in air) suggestive of not only binding of CQDs but also their deep penetration. Comparative CQD binding models were also used to fit the XR data (ESI,† Fig. S3) which were inferior to the best fit profile. Zn fluorescence detected at 8.6 keV in the X-ray fluorescence data, shown in Fig. 1(c), clearly confirms the presence of CQDs bound to the monolayer, which was absent in the case of XRF signals from the pristine O1G1 monolayer. From the analysed $\rho_s(z)$, it is not easy to discern any phase (raft) selective binding although we observe a slight increase in monolayer thickness which could be due to attractions between the CQD and the negatively charged DPPG head group as well as the negatively charged phosphate group in DOPC. To obtain an estimate of the extent of penetration, t_p, of the CQD core, one can subtract the CQD layer thickness beneath the monolayer (Table 1) from the core diameter of the CQD. In this case, t_p turns out to be $\sim$16 Å. The approximate coverage of the CQDs beneath the FLM was computed using the equation

$$\rho_{s\text{water}}(1-\phi_{QD})+\rho_{s\text{QD}}\times\phi_{QD}=\rho^{*}_{s\text{QD}}, \quad (4)$$

where $\rho_{s\text{water}}$ is the SLD of the bulk water in the subphase, ϕ_{QD} is the area fraction of the CQD layer/coverage area (refer Fig. 1 schematic) comprising the core/shell accompanying its ligands and $\rho^{*}_{s\text{QD}}$ is the effective SLD of the CQD layer obtained from the fit. ϕ_{QD} was found to be around 3%.

In order to explore the effect of CQD charge as well as the lipid headgroup interactions, which can be controlled by changing subphase pH, CQDs were also added below the O1G1 monolayer having the 1× PBS (buffer with pH 7) subphase. Fig. 2(a) shows normalized XR data and the corresponding fit using a 4-layer model (Fig. 1a, blue line fit) for the pristine FLM. A 2-layer model could not fit the data well (Fig. 2a, pink dashed line) and

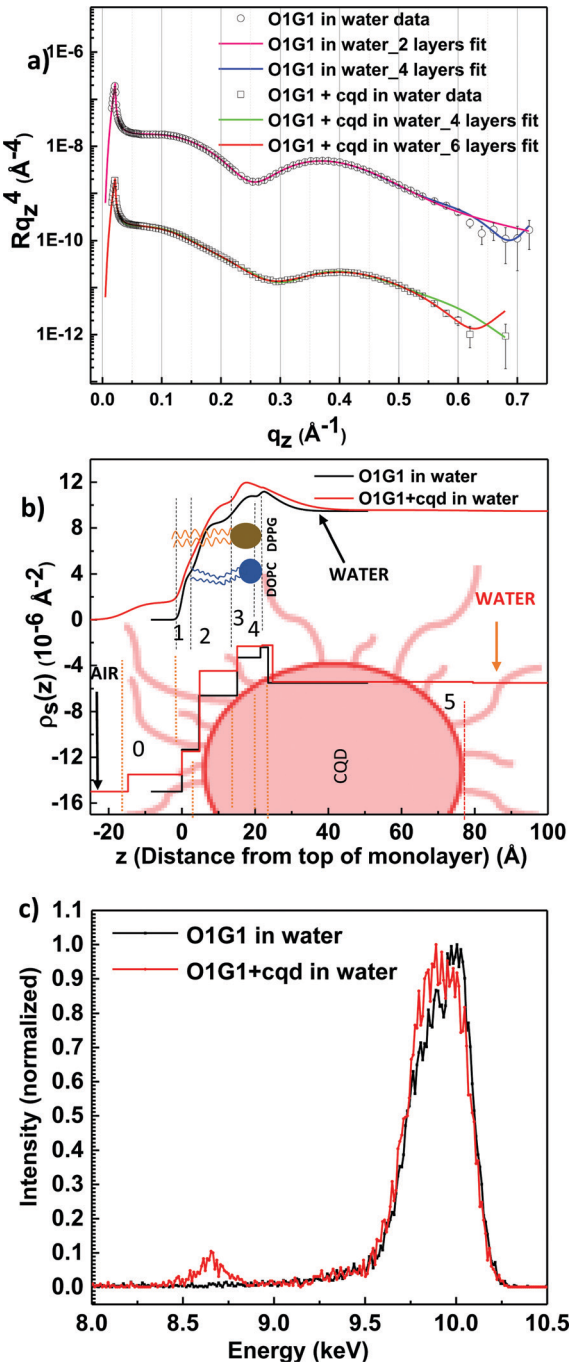

Fig. 1 (a) XR data of pristine DOPC : DPPG (1 : 1)/O1G1 and after adding CQDs in the water subphase. The pink and blue solid lines show fit to the pristine data using 2 and 4 layers respectively, the green solid line shows fit to the O1G1 + cqd data with 4 layers assuming there is no CQD layer beneath and the red solid line is the best fit to the O1G1 + cqd data with 6 layers assuming the CQD has penetrated the free lipid monolayer (FLM). (b) Smeared (top) and unsmeared (bottom) scattering length density (SLD) profiles before (corresponding to blue line fit in (a)) and after adding 10 nM CQD (corresponding to red line fit in (a)). The profile begins with air (left), followed by Tail1, Tail2, Head1 and Head2 layers and then bulk water for the pristine FLM. The layer numbers refer to those mentioned in Table 1. (c) X-ray fluorescence (XRF) data taken from the pristine O1G1 FLM in the pure DI water subphase (black) and O1G1 + cqd data (red) in Grazing Incidence Diffraction (GID) geometry.

Table 1 Parameters obtained from the XR fits of the O1G1 and P2G1 monolayers

Sample	$l_{Ligand1}$[a] (Å)	l_{Tail1} (Å)	l_{Tail2} (Å)	l_{Head1} (Å)	l_{Head2} (Å)	l_{CQD} (Å)	$l_{Ligand2}$	θ_t[b] (°)
O1G1 in DI water subphase (pH 6)		4.67 (3.67)[c]	10.44 (8.39)	6.35 (11.69)	2.07 (12.59)			38.1
After CQD	14.72 (1.49)	4.85 (3.52)	10.26 (10.52)	6.82 (12.68)	2.83 (12.77)	54.74 (9.55)		38.1
O1G1 in PBS subphase (pH 7)		5.59 (3.07)	11.22 (8.61)	8.32 (11.63)	3.08 (10.35)			28.9
After CQD		5.34 (1.31)	11.83 (8.08)	7.27 (12.07)	4.97 (11.13)	74.86 (9.72)	79.9 (9.71)	26.6
P2G1 in PBS subphase (pH 7)		3.71 (2.1)	12.89 (6.77)	9.03 (13.14)	2.69 (11.67)			30.2 [47.8][d]
After CQD	16.52 (1.1)	5.03 (3.65)	13.4 (9.59)	8.03 (13.42)	2.34 (12.28)	62.63 (9.77)	68.35 (9.61)	16.3 [45.7]

[a] Values in $l_{Ligand1}$, l_{Tail1}, l_{Tail2}, l_{Head1}, l_{Head2}, l_{CQD} and $l_{Ligand2}$ columns are the thicknesses of the slabs mentioned in the respective subscripts and these correspond to the slab numbers 0, 1, 2, 3, 4, 5, and 6 respectively in the best fit models illustrated in Fig. 1–3 schematics. [b] θ_t is the tilt angle of the lipid tails from the normal to the air–water interface. [c] Figures in brackets are the scattering length density values in 10^{-6} Å^{-2}. [d] Figures in [] are the tilt angles of the DPPC tails while those outside [] are the tilt angles of DPPG tails in the P2G1 monolayer.

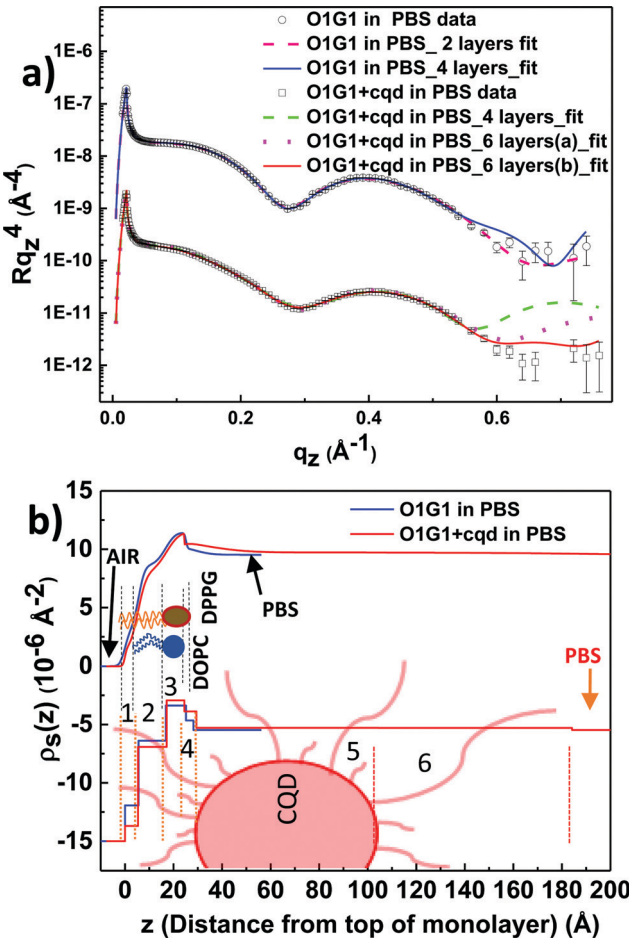

Fig. 2 (a) XR data of pristine DOPC : DPPG (1 : 1)/O1G1 and after adding CQDs in the 1× PBS subphase. The pink dashed line and the blue solid line show fit to the pristine data using 2 and 4 layers respectively, the green dashed line shows fit to the O1G1 + cqd data with 4 layers assuming there is no CQD layer beneath, the magenta dotted line shows fit with 6 layers assuming the CQD core has penetrated the FLM, and the red solid line is the best fit to the O1G1 + cqd data with 6 layers assuming the CQD core is just beneath the FLM with the ligands penetrating the FLM. (b) Smeared (top) and unsmeared (bottom) scattering length density (SLD) profiles before (corresponding to blue line fit in (a)) and after adding 10 nM CQD (corresponding to red line fit in (a)). The profile begins with air (left), followed by Tail1, Tail2, Head1 and Head2 layers and then bulk water for the pristine FLM. The layer numbers refer to those mentioned in Table 1.

the fit improved after using a 4-layer model reducing the χ^2 value of the fit to 14.05 from 18.14 for the 4-layer fit. In the PBS subphase, ΔH between the L_o and L_d phases was found to be 8.66 Å, which is higher compared to that in the water subphase (Table 1). This suggests that the higher pH seems to have affected the headgroup interaction more strongly for the DPPG phase compared to the DOPC phase. For the XR data after addition of CQDs, clear evidence of CQD binding was observed, since a 4 layer model did not fit the corresponding XR data very well (Fig. 2(a)). Interestingly, even a 6-layer model assuming that the CQD core has penetrated the FLM could not fit (magenta dotted line) the data well as compared to the model which considered that the CQD core was just below the FLM. The competitive models along with their schematics are illustrated in the ESI.† In fact, from eqn (4), we find a higher CQD coverage (~7%) beneath the monolayer as compared to that in water. This is also clearly evident from the higher ρ_s of this layer (Table 1) as well as from the intensity of the Zn peak in XRF data (ESI,† Fig. S2a). The higher density of adsorbed CQDs for similar sub-phase bulk density beneath the monolayer, probably, arises from the reduced charge on the CQDs as well as increased screening due to the presence of counterions allowing their closer packing. What is evident from the $\rho_s(z)$ profiles in Fig. 2(b), however, is the clear preferential interaction of CQDs with the DPPG containing charged ordered phase for which the headgroup thickness increases significantly (Table 2) while the disordered phase is not perturbed significantly. This is opposite to the observed behaviour for phase-separated uncharged membranes interacting with charged CQDs.[18,44,59] The ρ_s of the CQD ligands is larger compared to that of the bulk PBS aqueous subphase as found from the XR analysis (Table 1). In the pristine monolayer there are interpenetrating water molecules[74–76] (having lower ρ_s

Table 2 Parameters obtained from X-ray reflectivity data analyses

Sample	δt (Å) [in %]	ϕ_{QD} [in %]	δ(H2) [in %]
O1G1 in water subphase	1.07 [4.5]	3	37
O1G1 in PBS subphase (pH 7)	1.17 [4.1]	7	61.4
P2G1 in PBS subphase (pH 7)	0.5 [1.8]	10.1	−13

δt = change in monolayer thickness after CQD binding. ϕ_{QD} = coverage area of CQDs beneath the monolayer. δ(H2) = relative change in the Head2 (Table 1) thickness after CQD binding.

compared to that of the lipid heads) amongst the heads which lower the effective SLD of the head layers. With the CQD ligands penetrating the PG heads, it is possibly the case that many interpenetrating water molecules are replaced by the higher ρ_s ligands which effectively increases the ρ_s of the head layer. At the same time, we do not observe any significant penetration of the CQD core although there is increased disordering of the monolayer as evident from the reduced ρ_s in the tail layers. To incorporate the penetrating ligands, the tilt angles of the DPPG tails reduced to a certain extent (Table 1). The tilt angle from the normal to the interface was calculated by using the equation

$$\theta_t = \cos^{-1}\frac{l_{tail}}{19.2}, \quad (5)$$

where l_{tail} is the thickness of the 16-carbon tail obtained from the XR fit (l_{tail} of DPPG = l_{tail1} + l_{tail2} and l_{tail} of DPPC = l_{tail2}). The thickness of the untilted tail is considered to be 19.2 Å.[76] The reduced penetration could be due to reduced charge on CQDs as well as screening due to counterions beneath the O1G1 monolayer. The presence of counterions is further confirmed by the appearance of potassium, chloride and phosphate counterionic layers as can be inferred from the 2 keV phosphorus, 2.6 keV Chlorine and 3.3 keV potassium peaks in the XRF spectrum (inset of ESI,† Fig. S2a), which were not observed in the XRF spectrum for O1G1 in water. This, probably, prevented the CQDs from disrupting the mixed monolayer to the extent they did in the water subphase.

In the next system we investigate here, P2G1, we replaced the fluidic part, *i.e.* DOPC, with an ordered lipid, DPPC, keeping the charged lipid (DPPG) the same as in the earlier measurements and repeated the experiment. From the pressure-area isotherms (ESI,† Fig. S6a), it is evident that this monolayer has a lower area per lipid compared to O1G1, which is indicative of a higher packing density of the zwitterionic lipid phase as well as possibly an enhanced charged density of the DPPG phase. Fig. 3(a) shows the normalized XR data and the corresponding best fit. Similar to O1G1 on PBS the pristine P2G1 XR data collected at 26 mN m^{-1} could be well fit using a 4-layer model (Fig. 3a, blue line fit) with the corresponding $\rho_s(z)$ shown in Fig. 3(b). Once again we observed a small height difference ΔH of 1 Å between domains with the more ordered and thicker domain corresponding to DPPG. Although the pristine P2G1 FLM was modelled using 2 head layers, at this point it is difficult to conclusively comment on which lipid head has a larger thickness. From single-component monolayer studies on DPPC and DPPG, the PC and PG head can have a range of thicknesses with different orientations depending upon the surface pressure and temperature.[72–74] The CQDs were added to the mixed membrane P2G1 at 26 mN m^{-1} and 20 °C on the PBS subphase maintained at pH 7. A 4-layer model with no CQD layer was allowed to fit the P2G1 + cqd data, but the fit was not satisfactory (Fig. 3a, green dashed line fit) while a 7-layer model, as illustrated through Fig. 3c schematic, could best fit the data. So, there was definite CQD binding, which was also verified by the strong Zn peak from the XRF spectrum (ESI,† Fig. S2b). Interestingly, the 6 layer model which worked for O1G1 on PBS

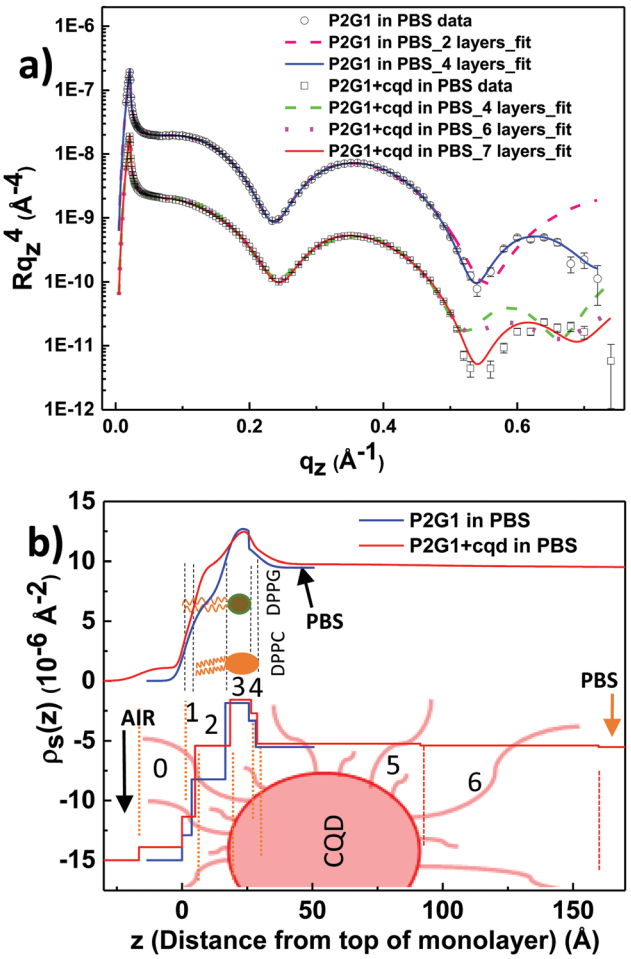

Fig. 3 (a) XR data of pristine DPPC : DPPG (2 : 1)/P2G1 and after adding CQDs in the 0.5× PBS subphase. The pink dashed line and the blue solid line show fit to the pristine data using 2 and 4 layers, the green dashed line shows fit to the O1G1 + cqd data with 4 layers assuming there is no CQD layer beneath, the magenta dotted line shows fit with 6 layers assuming the CQD core is just below the FLM and the red solid line is the best fit to the O1G1 + cqd data with 7 layers assuming the CQD has penetrated the FLM. (b) Smeared (top) and unsmeared (bottom) scattering length density (SLD) profiles before (corresponding to blue line fit in (a)) and after adding 10 nM CQD (corresponding to red line fit in (a)). The pristine P2G1 profile begins with air (left), followed by Tail1, Tail2, Head1 and Head2 layers and then bulk water for the pristine FLM. The layer numbers refer to those mentioned in Table 1.

did not give the best fit (Fig. 3a, magenta dotted line). From the fit parameters, only a 0.5 Å increase (Table 2) in the FLM thickness could be seen. On comparing with O1G1 + cqd data taken on the PBS subphase, the ligands were able to disrupt the DPPG tails because the other lipid component being a disordered and highly fluidic lipid (ESI,† Fig. S6), there was a large room for the DPPG tails to get disrupted and the DPPG domains to expand into the liquid-ordered DOPC-rich domains (ESI,† Fig. S7). In contrast, in P2G1, both the lipids are ordered, making the entire mixed monolayer to be a very compact one (ESI,† Fig. S6); hence the tails had no room to become disrupted. In fact, θ_t of the lipids, especially DPPG, is found to decrease (Table 1) which is a clear indication of the tails getting orientationally ordered. Notably, the

θ_t of DPPG lipids reducing considerably as compared to DPPC also suggests a preferential binding onto the charged DPPG phase. However, unlike the O1G1 on PBS case we do seem to observe some penetration of CQDs into the monolayer, $t_p \sim 8$ Å. This penetration is smaller than that observed with O1G1 on water but larger compared to the same monolayer on PBS. At this stage it is not clear what causes this higher penetration. However, we will discuss this aspect after considering the GID data.

Table 2 suggests that on the PBS subphase CQDs have a higher value of ϕ_{QD} below the P2G1 monolayer compared to that below O1G1. This might seem contrary to previous study by Roobala *et al.*,[18] where it was shown that the charged nanoparticles have preferential binding as well as higher penetration into the disordered and more fluidic phase present in a two-component lipid bilayer. However, the ordered component in that case was uncharged. In this case, for the P2G1 monolayer the more ordered lipid component is negatively charged and has a higher charge density (suggested from lower area per lipid in ESI,† Fig. S6a), which possibly leads to higher adsorption and penetration of CQDs compared to O1G1. Table 2 suggests that there was a 13% reduction in the Head2 layer. This can only happen if the positively charged QDs repel the exposed positive choline part of the PC headgroups away from the subphase and compel them to shrink. This implies that the Head2 layer extended into the subphase probably comprises the DPPC headgroup. So, there are implications for DPPC binding apart from the obvious DPPG binding, PG being negatively charged. Such behaviour of the zwitterionic PC headgroup in the proximity of charged species is well-known as already reported.[13,17] However, the scenario of preferential binding and other minute structural aspects of the consequences of CQD penetration shall be discussed in the GID section.

3.2 Grazing incidence diffraction (GID) measurements

Apart from the XR measurements, GID was performed on the same set of monolayers to collect information about the effect of the CQDs on the lattice structural changes of the ordered lipid components in the FLMs. It has been shown earlier that a pure DPPG monolayer has a single peak on water at higher pressures around 32 mN m^{-1} indicating a hexagonal lattice which gets distorted to produce 2 non-degenerate diffracted peaks on the PBS subphase or at lower surface pressures.[72,73,77,78] Our data on O1G1 FLMs at 32 mN m^{-1} also showed a similar behaviour (ESI,† Fig. S8 and S9).

Fig. 4a shows GID data for the O1G1 monolayer on the DI water subphase at 26 mN m^{-1} which primarily originates from the ordered and negatively charged DPPG containing L_o domains. Two peaks were observed, consistent with earlier observations on pristine DPPG monolayers at lower pressure.[73,78] The lower Q_{xy} peak is centred at $Q_Z > 0$ (ESI,† Fig. S11) which suggests a transformation from an undistorted hexagonal lattice at 32 mN m^{-1} to a centred rectangular lattice at 26 mN m^{-1} with the lattice parameters as shown in Table 3.

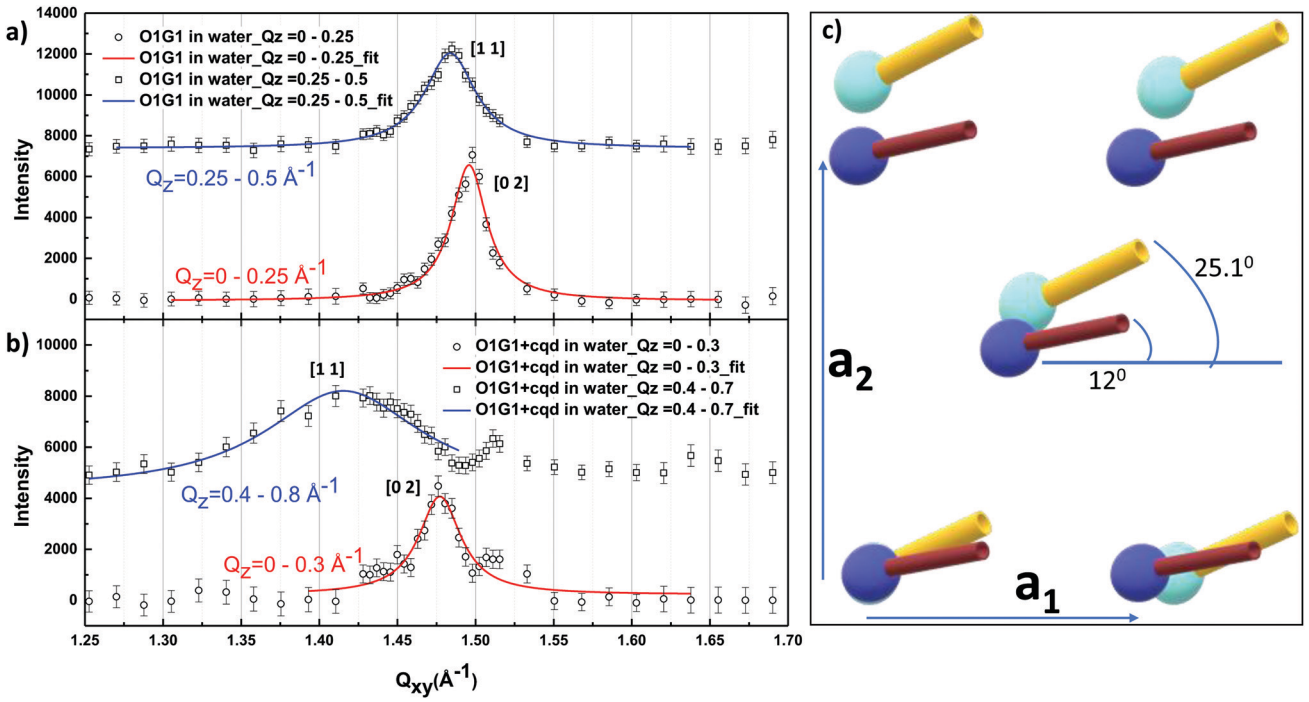

Fig. 4 GID data of (a) pristine DOPC : DPPG (1 : 1) monolayer and (b) after adding 10 nM CQDs, collected at 26 mN m^{-1} and 20 °C in the DI water subphase, showing significant lattice distortion in the ordered DPPG lattice. The [11] and [02] Bragg reflection intensities have been integrated through specific Q_z ranges as depicted in the graphs, and have been shifted vertically for clarity. (c) Schematic showing the top view of the DPPG centred-rectangular lattice present in the pristine O1G1 FLM in the DI water (pH 6) subphase (dark blue balls and brown rods) and the expanded lattice after CQD binding (light blue balls with yellow rods) showing the azimuthal tilt towards the nearest neighbour.

Table 3 Parameters obtained from GID data analyses

Sample	a (Å)	b (Å)	L_{xy}[11][a] (Å)	L_{xy}[02][a] (Å)	A_h[b] (Å^2)	θ_{NN}[c] (°)	L_z[a]	d_n[d] (nm^2)
O1G1 in DI water (pH 6)	4.9	8.4	148.8 ± 6.6	225.8 ± 15.9	41.2	12.0 ± 0.4	15.4 ± 1.6 [9.5 ± 0.7][e]	161.7
After CQD	5.2	8.5	46.5 ± 6.2	184.8 ± 27.8	44.3 ± 0.2	25.1 ± 0.4	36.4 ± 5.1 [11 ± 1]	36
O1G1 in PBS (pH 7)	5.15 ± 0.01	8.46	63.4 ± 9.0	210.3 ± 30.0	43.6 ± 0.1	20.8 ± 0.4	15.1 ± 4.0 [8.8 ± 1.0]	56.3
After CQD	5.28	8.48	70.4 ± 7.4	325.8 ± 79.9	44.8 ± 0.1	28.9 ± 0.5	13.8 ± 4.1 [13.4 ± 1.3]	96.9
P2G1 in PBS (pH 7)	4.95 (5.54)[f]	8.57 (8.57)	70.8 ± 2.7	302.4 ± 10.4	42.4 (47.5)	0 (32.3 ± 0.2)	18.6 ± 0.8 [15.3 ± 0.8]	718.2 (93.2)
After CQD	4.95 (5.54)	8.57 (8.57)	71.0 ± 2.6	285.5 ± 13.4	42.4 (47.5)	0 (32.8 ± 0.2)	18.5 ± 0.7 [15.7 ± 0.9]	640.2 (88.4)

The lattice parameters without the standard deviation errors are precise to the least significant digit. [a] L_{xy}[11], L_{xy}[02], and L_z are the in-plane coherence lengths along the [11] and [02] lattice vectors and the out-of-plane coherence length for the Bragg rods respectively. [b] A_h is the DPPG head-group area in O1G1, and individual head-group area of DPPC and DPPG in P2G1 nanodomains. [c] Azimuthal angles of the tail tilt towards the Nearest Neighbour (NN) in the centred-rectangular lattice. [d] d_n = nanodomain sizes. [e] Values in [ ] denote the out-of-plane coherence lengths for the [02] Bragg rod while those outside [ ] correspond to the [11] Bragg rods. [f] The figures in brackets denote the parameters of the DPPC lattice in P2G1, and the figures outside brackets denote the parameters of the DPPG lattice.

Earlier studies have used GID measurements on mixed FLMs containing raft-like domains to estimate these nanodomain sizes,[71] d_n. On account of having asymmetric coherence lengths, L_{xy}, estimated from the respective GID peaks, in Fig. 4a, along [02] and [11] lattice vectors (Table 3), the DPPG-rich scattering entity is considered to be an ellipsoidal raft/nanodomain. These nanodomains are believed to be floating in the background of a fluidic L_d phase consisting mostly of DOPC lipids. The estimated d_n values are also indicated in Table 3. Fig. 4b shows the GID data collected from O1G1 (on the DI water subphase) after addition of CQDs. The data show considerable modification in both the [02] and [11] peaks. The lattice expands significantly leading to an increase in area per molecule, A_h, as indicated in Table 3. But most interestingly, we observe a strong reduction of d_n from 161.7 nm^2 to 36 nm^2 suggesting disruption of rafts. On the DI water subphase, the CQDs are seen to affect the DPPG tails by increasing their tilt (azimuthal angles) (θ_{NN}) significantly from 12° to 25.1° towards the nearest neighbour (NN) DPPG molecule in the lattice (Fig. 4c). While GID data indicate strong interaction with the L_o phase containing DPPG, the preferential binding cannot be inferred since the DOPC containing L_d phase does not give rise to any peaks in GID. From Table 3, the out-of-plane coherence length, $\mathbf{L_z}$, estimated from the width of the [11] Bragg rod (ESI,† Fig. S11), increased from 15.4 Å to 36.4 Å. It is possible that this enhanced $\mathbf{L_z}$ could emerge due to the CQD ligands (which are longer) which are interspersed with the lipid tails. It can be noted that analysis of the corresponding XR data suggested the possible presence of a ligand layer, fully penetrating the FLM, consistent with the above observation from GID.

For the O1G1 FLM on PBS, the peaks were found to have a low intensity in contrast to the DI water subphase because of the high background created by the X-ray scattered from the counterionic layer beneath the FLM (ESI,† Fig. S12). For the pristine O1G1 FLM on PBS, A_h is larger while the respective L_{xy} values are much smaller (Table 3), compared to the O1G1 FLM on water, suggesting a looser packing of lipids. Also, d_n is considerably smaller compared to the O1G1 FLM on DI water. On addition of CQDs, the observed increase in A_h is much smaller indicating weaker interaction and reduced penetration, consistent with the information obtained from the corresponding XR data analysis (Table 1). Intriguingly, we do observe a visible increase in the L_{xy} value of the [02] peak, leading to an increase in d_n suggesting coalescence of these domains due to CQD binding. Such coalescence must be mediated by the charge of the CQDs which implies the preference of these nanoparticles to bind to the anionic L_o phase. This observation is consistent with the increased head group thickness of the DPPG molecules present in the L_o phase as observed from XR.

Fig. 5a shows GID data for the pristine P2G1 monolayer at 26 mN m^{-1} and 20 °C. The scattering intensity was much higher compared to that from O1G1 monolayers and produced very strong [11] and [02] peaks. This could be understood from the fact that in P2G1, the entire monolayer area onto which the X-ray footprint is incident is highly ordered. Opposed to this, in the O1G1 monolayer, only a fraction of the monolayer – the DPPG nanodomains – was incoherently contributing to the cumulative intensity leading to the DPPG Bragg peaks. Large coherence lengths (Table 3) were observed along the [02] lattice vectors of the centred rectangular DPPG lattice. In fact, in this case the [02] peak was an amalgamated diffracted intensity arising from both the liquid-ordered DPPC grains and the DPPG grains. On the other hand, the coherence length along the [11] lattice vector is a consequence of the DPPC lattice only, because DPPC is well known from the literature to have 2 peaks.[75,77] This [11] peak is broader (implying a lower coherence length) than or comparable to that in O1G1 (on water) as in that case, the [11] peak arose from diffraction from the more ordered DPPG lattices. The information about θ_{NN} in DPPC and DPPG tails was extracted out from the Bragg peaks and the Bragg rods (ESI,† Fig. S13), the values of which are mentioned in Table 3. From the GID fit parameters, it is clear that after CQD binding to the P2G1 monolayer, there is a negligible change in the lattice vectors $\mathbf{a}_1$ and $\mathbf{a}_2$. However the intensity of the [11] and [02] peaks was found to decrease to a fraction 0.9 and 0.71 respectively after CQD addition. This suggests that the DPPG lattice had been more affected by the preferential binding of CQDs.

3.3 Discussion

There are two main aspects of our study of interaction of CQDs with phase-separated, charged lipid monolayers which emerge from the discussions above: varying penetration in these mixed FLMs and the phenomenon of preferential binding. Our study brings out the role of lipid packing and charge density of the

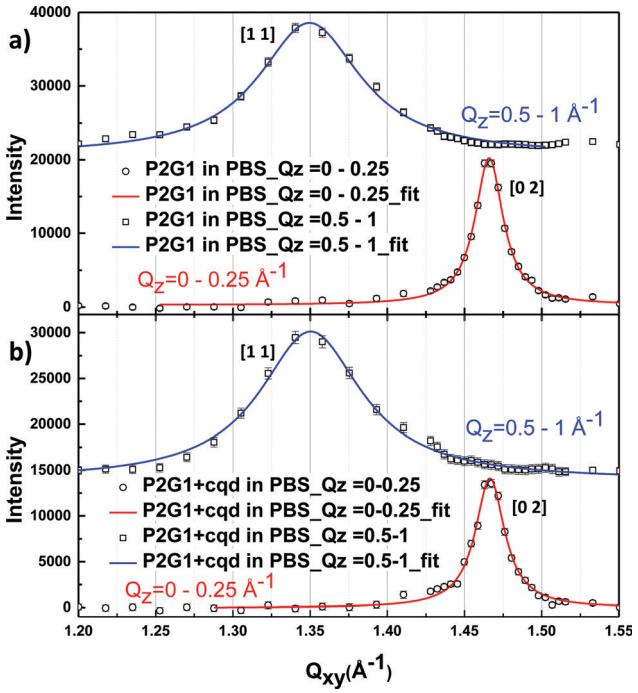

Fig. 5 GID data of (a) pristine DPPC : DPPG (2 : 1) and (b) after adding 10 nM CQDs, collected at 26 mN m^{-1} and 20 °C in the PBS subphase, showing minimal lattice distortion in the ordered DPPC and DPPG lattice. The [11] and [02] Bragg reflection intensities have been integrated through specific Q_z ranges as depicted in the graphs, and have been shifted vertically for clarity.

mixed FLMs which drive these biophysical phenomena at the nanoscale. The primary motive behind this investigation was to observe whether it is the entropy of the zwitterionic lipid component or the charge density of the membrane which determines the extent of binding and penetration of charged nanoparticles. In previous studies, it had been reported that charged nanoparticles prefer to bind to the more fluidic lipid phase in a two component zwitterionic membrane. In this study we have observed that in the case of O1G1 FLMs, the CQDs bind to the membrane and from the GID data analysis it is seen that the bound CQDs distort the ordered DPPG lattice and cause the θ_{NN} of the DPPG acyl chains to increase although no information can be obtained regarding their binding propensity to the more fluidic DOPC phase. This observation confirms that the CQDs bind to the anionic DPPG domains through strong electrostatic interaction. From the XR data analysis, it was observed that the CQDs bound to negatively charged DPPG head-groups and increased the thickness of the DPPG head layer but did not affect the DOPC layer thickness suggesting the possibility of preferential binding to the ordered but oppositely charged domains containing, predominantly, DPPG lipids. The salts present in the PBS buffer subphase for the O1G1 FLM play an important role because the counterionic layer formed beneath the monolayer was found to prevent the charged nanoparticles from infiltrating the monolayer leading to lower penetration and binding. In the case of water subphase, the nanoparticles have been found to penetrate the O1G1 monolayer to a greater extent. The subphase environment was also different in terms of pH and also impacted the charge density of the lipids as well as the charge on the CQD surface. The DI water, having a lower pH (= 6), increases the surface charge of the CQDs, and the monolayer, being fractionally negatively charged due its DPPG component, caused the higher charged CQDs to attack the mixed lipid membrane to a greater degree. The presence of counter-ions in the PBS subphase screened the charge of the CQDs, allowing them to come closer and cover a larger fraction of the area beneath the O1G1 membrane when present in the PBS subphase as compared to DI water. The changes are more dramatic in the DI water subphase (pH 6) as compared to PBS subphase (pH 7) because of the larger surface charge of CQDs at lower pH and also because the DPPG nanodomains, with a lower headgroup area, have a higher surface charge density of 2.427 e^- nm^{-2} in the DI water subphase compared to 2.294 e^- nm^{-2} in the PBS subphase. Although the isotherms of O1G1 FLMs suggest that the average area per lipid is lower on the PBS subphase compared to that on DI water (ESI,† Fig. S6a), the GID data suggest that the mean molecular area of the DPPG lipids alone is lower on the DI water subphase. This is expected because at lower pH, the positive counter-ions screen the negative charges of the lipid headgroup, allowing them to pack closely, thus increasing the charge density.[79] This also possibly explains the highest penetration by the CQDs into O1G1 on the DI water subphase as observed from the XR analyses. Replacing the fluidic zwitterionic component with an ordered lipid DPPC for the P2G1 system led to increased overall lipid packing and charge density. As a result we did not observe any significant change in the lattice parameters from GID data analysis after addition of CQDs. It has been studied that the CQDs reduce the line tension between the domains.[80] In this case too, the CQD core penetrates by around 10–12 Å and in the process, reduces the tension at the boundaries between the lipid nanodomains and reduces their size (Table 3). The CQDs possibly squeeze into the lipids and instead of causing disruption, induce more ordering in the tail region. This conforms with the XR results, where the tail electron densities were seen to increase – a clear indication of minimal disruption and more ordering in the plane normal to the air–water interface. This is due to the highly compact P2G1 monolayer (ESI,† Fig. S6b) which prevents the CQDs from causing disordering along the plane normal to the interface. This is the reason why the CQD binding is unable to produce lattice changes in the ordered nanodomains but merely reduces the d_n. The mean molecular area of DPPG in P2G1 is less than that in O1G1 (in PBS). GID analysis also suggests that DPPG nanodomains in P2G1 have a surface charge density of 2.358 e^- nm^{-2} which is higher than that in the O1G1 FLM (on the PBS subphase). This suggests why penetration of the CQDs was found to be more in the case of P2G1 on PBS as compared to O1G1 on the same subphase. Further, the intensity of the Bragg peak arising from the DPPG lattices reduces by a larger fraction compared to the other peak arising from DPPC domains after CQD binding. Moreover, θ_t of DPPG tails was observed to reduce considerably, while DPPC tilt angles did not alter much. This indicates that in such an ordered membrane too, the CQDs prefer

DPPG domains to bind to. On the same PBS subphase (pH 7), a striking difference between O1G1 and P2G1 was that the CQDs caused the DPPG rafts to coalesce in the O1G1 FLM whereas in P2G1, the CQDs reduced both the DPPC and DPPG raft sizes. In O1G1 the phenomenon of raft coalescence is predominant and seems to lead to enlargement of the negatively charged rafts. It is also noteworthy that d_n of the anionic DPPG nanodomains in P2G1 is 12.75 times larger compared to that of the nanodomains present in O1G1. Although the mole fraction of the anionic DPPG molecules in P2G1 is less (as compared to O1G1), such strikingly larger anionic d_n in P2G1 with a higher charge density has probably led to a larger coverage of the CQDs beneath the P2G1 monolayer as observed from the XR analyses.

4 Conclusions

In conclusion, using a combination of XR, GID and XRF techniques we provide microscopic insight into the nature of charged nanoparticle interaction with mixed zwitterionic and negatively charged lipid membranes, especially their ability to penetrate and bind in a phase specific manner. Contrary to earlier reports, we observe higher preference of QD binding to the more ordered but negatively charge phase. Further, the density of the adsorbed CQD layer as well as their ability to penetrate the lipid monolayer biomembranes could be tuned by changing ambient pH and the stiffness and structural ordering of the zwitterionic lipid component. Our study also reveals the presence of membrane nanodomains and indicates how they are perturbed by CQD interaction due to the subtle interplay of entropic and electrostatic effects. We believe this will help the future research in designing specific nanoparticles to target cell membranes with different electrolytic environments and mechano-electrostatic properties for bio-imaging and targeted drug delivery as well as in providing directions to mitigate nanoparticle induced respiratory diseases due to their cytotoxic effects. In general, the results presented here could be also relevant in understanding the interactions of other pathogens like viruses or charged biomolecules, which are typically of tens of nanometres in dimension, with cells.

Author contributions

J. K. B. and N. R. J. conceptualized the study. The beamline experiments were performed by A. C. under the supervision of J. K. B. and with assistance from W. B. The synthesis and characterization of the CQDs were performed by K. D. The analysis of the X-ray reflectivity, Grazing Incidence Diffraction and X-ray Fluorescence was performed by A. C. through inputs from J. K. B. and W. B. The first draft was written by A. C. and modified by J. K. B. with inputs from all the authors.

Conflicts of interest

There are no conflicts to declare.

Acknowledgements

The authors thank the Department of Science and Technology, India (SR/NM/Z-07/2015) for the financial support and the Jawaharlal Nehru Centre for Advanced Scientific Research (JNCASR) for managing the project. NSF's ChemMatCARS Sector 15 is supported by the Divisions of Chemistry (CHE) and Materials Research (DMR), National Science Foundation, under grant number NSF/CHE-1834750. Use of the Advanced Photon Source, an Office of Science User Facility operated for the U.S. Department of Energy (DOE) Office of Science by Argonne National Laboratory, was supported by the U.S. DOE under Contract No. DE-AC02-06CH11357. The authors are also thankful to Mr Ravindra Kumar Yadav, IISc, for his help in the beamline experiments.

Notes and references

1 N. R. Jana, *Phys. Chem. Chem. Phys.*, 2011, **13**, 385–396.
2 A. Chakraborty and N. R. Jana, *J. Phys. Chem. Lett.*, 2015, **6**, 3688–3697.
3 S. J. Tan, N. R. Jana, S. Gao, P. K. Patra and J. Y. Ying, *Chem. Mater.*, 2010, **22**, 2239–2247.
4 C. Dalal and N. R. Jana, *J. Phys. Chem. B*, 2017, **121**, 2942–2951.
5 D. Chenthamara, S. Subramaniam, S. G. Ramakrishnan, S. Krishnaswamy, M. M. Essa, F.-H. Lin and M. W. Qoronfleh, *Biomater. Res.*, 2019, **23**, 1–29.
6 Z. Xue, Q. Sun, L. Zhang, Z. Kang, L. Liang, Q. Wang and J.-W. Shen, *Nanoscale*, 2019, **11**, 4503–4514.
7 S. Parimi, T. J. Barnes and C. A. Prestidge, *Langmuir*, 2008, **24**, 13532–13539.
8 A. Mecke, S. Uppuluri, T. M. Sassanella, D.-K. Lee, A. Ramamoorthy, J. R. Baker Jr, B. G. Orr and M. M. B. Holl, *Chem. Phys. Lipids*, 2004, **132**, 3–14.
9 R. Bhattacharya, S. Kanchi, C. Roobala, A. Lakshminarayanan, O. H. Seeck, P. K. Maiti, K. Ayappa, N. Jayaraman and J. K. Basu, *Soft Matter*, 2014, **10**, 7577–7587.
10 E.-K. Lim, B. H. Chung and S. J. Chung, *Curr. Drug Targets*, 2018, **19**, 300–317.
11 A. E. Nel, L. Mädler, D. Velegol, T. Xia, E. M. Hoek, P. Somasundaran, F. Klaessig, V. Castranova and M. Thompson, *Nat. Mater.*, 2009, **8**, 543–557.
12 M. Schulz, A. Olubummo and W. H. Binder, *Soft Matter*, 2012, **8**, 4849–4864.
13 B. Wang, L. Zhang, S. C. Bae and S. Granick, *Proc. Natl. Acad. Sci. U. S. A.*, 2008, **105**, 18171–18175.
14 M. Laurencin, T. Georgelin, B. Malezieux, J.-M. Siaugue and C. Ménager, *Langmuir*, 2010, **26**, 16025–16030.
15 N. Biswas, R. Bhattacharya, A. Saha, N. R. Jana and J. K. Basu, *Phys. Chem. Chem. Phys.*, 2015, **17**, 24238–24247.
16 A. Olubummo, M. Schulz, B.-D. Lechner, P. Scholtysek, K. Bacia, A. Blume, J. Kressler and W. H. Binder, *ACS Nano*, 2012, **6**, 8713–8727.
17 A. Velikonja, P. B. Santhosh, E. Gongadze, M. Kulkarni, K. Eleršič, Š. Perutkova, V. Kralj-Iglič, N. P. Ulrih and A. Iglič, *Int. J. Mol. Sci.*, 2013, **14**, 15312–15329.

18 R. Chelladurai, K. Debnath, N. R. Jana and J. K. Basu, *Langmuir*, 2018, **34**, 1691–1699.
19 M. Yu, C. Zhou, J. Liu, J. D. Hankins and J. Zheng, *J. Am. Chem. Soc.*, 2011, **133**, 11014–11017.
20 H.-M. Ding and Y.-Q. Ma, *Sci. Rep.*, 2013, **3**, 2804.
21 Y. Hu, T. Litwin, A. R. Nagaraja, B. Kwong, J. Katz, N. Watson and D. J. Irvine, *Nano Lett.*, 2007, **7**, 3056–3064.
22 P. Loganathan and M. M. Magzoub, *Biophys. J.*, 2020, **118**, 477a.
23 P. Swietach, R. D. Vaughan-Jones, A. L. Harris and A. Hulikova, *Philos. Trans. R. Soc., B*, 2014, **369**, 20130099.
24 B. A. Webb, M. Chimenti, M. P. Jacobson and D. L. Barber, *Nat. Rev. Cancer*, 2011, **11**, 671–677.
25 J.-H. Lee, J.-T. Jang, J.-S. Choi, S. H. Moon, S.-H. Noh, J.-W. Kim, J.-G. Kim, I.-S. Kim, K. I. Park and J. Cheon, *Nat. Nanotechnol.*, 2011, **6**, 418–422.
26 J. M. Jagtap, A. K. Parchur and G. Sharma, *Intelligent Nanomaterials for Drug Delivery Applications*, Elsevier, 2020, pp. 43–59.
27 A.-R. Lupu, T. Popescu and M. Stojanović, *Environmental Nanotechnology*, Springer, 2020, vol. 3, pp. 47–87.
28 G. Canavese, A. Ancona, L. Racca, M. Canta, B. Dumontel, F. Barbaresco, T. Limongi and V. Cauda, *Chem. Eng. J.*, 2018, **340**, 155–172.
29 O. K. Kosheleva, T.-C. Lai, N. G. Chen, M. Hsiao and C.-H. Chen, *J. Nanobiotechnol.*, 2016, **14**, 46.
30 Z. Ashikbayeva, D. Tosi, D. Balmassov, E. Schena, P. Saccomandi and V. Inglezakis, *Nanomaterials*, 2019, **9**, 1195.
31 R. K. Harishchandra, M. Saleem and H.-J. Galla, *J. R. Soc., Interface*, 2010, **7**, S15–S26.
32 D. Kondej and T. R. Sosnowski, *Environ. Sci. Pollut. Res.*, 2016, **23**, 4660–4669.
33 J. J. Schüer, C. Wölk, U. Bakowsky and S. R. Pinnapireddy, *Colloids Surf., B*, 2020, **188**, 110750.
34 J. J. Schüer, A. Arndt, C. Wölk, S. R. Pinnapireddy and U. Bakowsky, *Langmuir*, 2020, **36**, 4808–4819.
35 K. Yue, X. Sun, J. Tang, Y. Wei and X. Zhang, *Int. J. Mol. Sci.*, 2019, **20**, 3281.
36 S. I. Hossain, N. S. Gandhi, Z. E. Hughes, Y. Gu and S. C. Saha, *Biochim. Biophys. Acta, Biomembr.*, 2019, **1861**, 1458–1467.
37 A. Verma and F. Stellacci, *Small*, 2010, **6**, 12–21.
38 X. C. He, M. Lin, F. Li, B. Y. Sha, F. Xu, Z. G. Qu and L. Wang, *Nanomedicine*, 2015, **10**, 121–141.
39 S. Sharifi, S. Behzadi, S. Laurent, M. L. Forrest, P. Stroeve and M. Mahmoudi, *Chem. Soc. Rev.*, 2012, **41**, 2323–2343.
40 A. Chakraborty, C. Dalal and N. R. Jana, *Langmuir*, 2018, **34**, 13461–13471.
41 E. Rascol, J.-M. Devoisselle and J. Chopineau, *Nanoscale*, 2016, **8**, 4780–4798.
42 N. Azman, L. Bekale, T. X. Nguyen and J. C. Y. Kah, *Nanoscale*, 2020, **12**, 14021–14036.
43 E. S. Melby, A. C. Mensch, S. E. Lohse, D. Hu, G. Orr, C. J. Murphy, R. J. Hamers and J. A. Pedersen, *Environ. Sci.: Nano*, 2016, **3**, 45–55.
44 A. C. Mensch, E. S. Melby, E. D. Laudadio, I. U. Foreman-Ortiz, Y. Zhang, A. Dohnalkova, D. Hu, J. A. Pedersen, R. J. Hamers and G. Orr, *Environ. Sci.: Nano*, 2020, **7**, 149–161.
45 S. Nangia and R. Sureshkumar, *Langmuir*, 2012, **28**, 17666–17671.
46 T. Pfeiffer, A. De Nicola, C. Montis, F. Carla, N. F. van der Vegt, D. Berti and G. Milano, *J. Phys. Chem. Lett.*, 2018, **10**, 129–137.
47 A. Ridolfi, L. Caselli, C. Montis, G. Mangiapia, D. Berti, M. Brucale and F. Valle, *J. Microsc.*, 2020, DOI: 10.1111/jmi.12910.
48 O. Borozenko, M. Faral, S. Behyan, A. Khan, J. Coulombe, C. DeWolf and A. Badia, *ACS Appl. Nano Mater.*, 2018, **1**, 5268–5278.
49 S. L. Selladurai, R. Miclette Lamarche, R. Schmidt and C. E. DeWolf, *Langmuir*, 2016, **32**, 10767–10775.
50 L. Wang, P. Quan, S. H. Chen, W. Bu, Y.-F. Li, X. Wu, J. Wu, L. Zhang, Y. Zhao and X. Jiang, *et al.*, *ACS Nano*, 2019, **13**, 8680–8693.
51 S. S. You, C. T. Heffern, Y. Dai, M. Meron, J. M. Henderson, W. Bu, W. Xie, K. Y. C. Lee and B. Lin, *J. Phys. Chem. B*, 2016, **120**, 9132–9141.
52 M. Paulus, P. Degen, T. Brenner, S. Tiemeyer, B. Struth, M. Tolan and H. Rehage, *Langmuir*, 2010, **26**, 15945–15947.
53 E. M. Curtis, A. H. Bahrami, T. R. Weikl and C. K. Hall, *Nanoscale*, 2015, **7**, 14505–14514.
54 R. Gupta, Y. Badhe, S. Mitragotri and B. Rai, *Nanoscale*, 2020, **12**, 6318–6333.
55 S. Wang, H. Guo, Y. Li and X. Li, *Nanoscale*, 2019, **11**, 4025–4034.
56 S. Tatur, M. Maccarini, R. Barker, A. Nelson and G. Fragneto, *Langmuir*, 2013, **29**, 6606–6614.
57 D. Di Silvio, M. Maccarini, R. Parker, A. Mackie, G. Fragneto and F. B. Bombelli, *J. Colloid Interface Sci.*, 2017, **504**, 741–750.
58 S. Srivastava, D. Nykypanchuk, M. Fukuto and O. Gang, *ACS Nano*, 2014, **8**, 9857–9866.
59 A. C. Mensch, J. T. Buchman, C. L. Haynes, J. A. Pedersen and R. J. Hamers, *Langmuir*, 2018, **34**, 12369–12378.
60 M. Schulz and W. H. Binder, *Macromol. Rapid Commun.*, 2015, **36**, 2031–2041.
61 J. K. Sheavly, J. A. Pedersen and R. C. Van Lehn, *Nanoscale*, 2019, **11**, 2767–2778.
62 R. Chelladurai and J. K. Basu, *J. Phys. D: Appl. Phys.*, 2018, **51**, 304002.
63 S. Behyan, O. Borozenko, A. Khan, M. Faral, A. Badia and C. DeWolf, *Environ. Sci.: Nano*, 2018, **5**, 1218–1230.
64 S. Basiruddin, A. Saha, N. Pradhan and N. R. Jana, *Langmuir*, 2010, **26**, 7475–7481.
65 A. Nelson, *J. Appl. Crystallogr.*, 2006, **39**, 273–276.
66 L. G. Parratt, *Phys. Rev.*, 1954, **95**, 359.
67 A. Guinier, *X-ray diffraction in crystals, imperfect crystals, and amorphous bodies*, Courier Corporation, 1994.
68 K. Kjaer, *Phys. B*, 1994, **198**, 100–109.
69 W. Bu, M. Mihaylov, D. Amoanu, B. Lin, M. Meron, I. Kuzmenko, L. Soderholm and M. L. Schlossman, *J. Phys. Chem. B*, 2014, **118**, 12486–12500.

70 M. K. Ratajczak, E. Y. Chi, S. L. Frey, K. D. Cao, L. M. Luther, K. Y. C. Lee, J. Majewski and K. Kjaer, *Phys. Rev. Lett.*, 2009, **103**, 028103.
71 F. Evers, C. Jeworrek, K. Weise, M. Tolan and R. Winter, *Soft Matter*, 2012, **8**, 2170–2175.
72 E. Y. Chi, C. Ege, A. Winans, J. Majewski, G. Wu, K. Kjaer and K. Y. C. Lee, *Proteins: Struct., Funct., Bioinf.*, 2008, **72**, 1–24.
73 D. Gidalevitz, Y. Ishitsuka, A. S. Muresan, O. Konovalov, A. J. Waring, R. I. Lehrer and K. Y. C. Lee, *Proc. Natl. Acad. Sci. U. S. A.*, 2003, **100**, 6302–6307.
74 M. Thoma, M. Schwendler, H. Baltes, C. A. Helm, T. Pfohl, H. Riegler and H. Möhwald, *Langmuir*, 1996, **12**, 1722–1728.
75 E. Watkins, C. Miller, D. Mulder, T. Kuhl and J. Majewski, *Phys. Rev. Lett.*, 2009, **102**, 238101.
76 C. Helm, H. Möhwald, K. Kjaer and J. Als-Nielsen, *EPL*, 1987, **4**, 697.
77 G. Wu, J. Majewski, C. Ege, K. Kjaer, M. J. Weygand and K. Y. C. Lee, *Biophys. J.*, 2005, **89**, 3159–3173.
78 F. Neville, Y. Ishitsuka, C. S. Hodges, O. Konovalov, A. J. Waring, R. Lehrer, K. Y. C. Lee and D. Gidalevitz, *Soft Matter*, 2008, **4**, 1665–1674.
79 S. Harguindey, D. Stanciu, J. Devesa, K. Alfarouk, R. A. Cardone, J. D. P. Orozco, P. Devesa, C. Rauch, G. Orive and E. Anitua, *et al.*, *Semin. Cancer Biol.*, 2017, 157–179.
80 D. L. Cheung, *J. Chem. Phys.*, 2014, **141**, 194908.

